

Fast thermal desorption spectroscopy study of morphology and vaporization kinetics of polycrystalline ice films

Haiping Lu, Stephanie A. McCartney, M. Chonde, D. Smyla, and Vlad Sadtchenko^{a)}
Department of Chemistry, The George Washington University, Washington, District of Columbia 20052

(Received 6 February 2006; accepted 16 May 2006; published online 27 July 2006;
 publisher error corrected 20 February 2007)

Fast thermal desorption spectroscopy was used to investigate the vaporization kinetics of thin (50–100 nm) H_2O^{18} and HDO tracer layers from 2–5 μm thick polycrystalline H_2O^{16} ice films at temperatures ranging from -15 to -2 °C. The isothermal desorption spectra of tracer species demonstrate two distinct peaks, α and β , which we attribute to the vaporization of H_2O^{18} initially trapped at or near the grain boundaries and in the crystallites of the polycrystalline ice, respectively. We show that the diffusive transport of the H_2O^{18} and HDO tracer molecules in the bulk of the H_2O^{16} film is slow as compared to the film vaporization. Thus, the two peaks in the isothermal spectra are due to unequal vaporization rates of H_2O^{18} from grain boundary grooves and from the crystallites and, therefore, can be used to determine independently the vaporization rate of the single crystal part of the film and rate of thermal etching of the film. Our analysis of the tracer vaporization kinetics demonstrates that the vaporization coefficient of *single crystal* ice is significantly greater than those predicted by the classical vaporization mechanism at temperatures near ice melting point. We discuss surface morphological dynamics and the bulk transport phenomena in single crystal and polycrystalline ice near 0 °C. © 2006 American Institute of Physics. [DOI: 10.1063/1.2212395]

I. INTRODUCTION

The physical chemistry of ice is of the utmost fundamental and applied significance. Indeed, ice is ubiquitously present in nature and plays a central role in a vast array of environmental processes. Examples of applied areas, which require knowledge of the physics and chemistry of various solid forms of water, include atmospheric chemistry and climate change, soil chemistry, planetary and interstellar chemistry, cryopreservation, and research into alternative energy sources. Furthermore, ice and water are uniquely accessible to computational modeling, due to the availability of extensive information on the intermolecular interactions in water-containing systems. Therefore, ice is often considered to be a model system for studies of fundamental properties of condensed molecular phases.

Past experimental studies of condensed phase physics and chemistry have been conducted mostly with “static” solids, such as metals and semiconductors at temperatures well below their melting points. Nevertheless, a multitude of important chemical and physical phenomena occur in confined molecular environments, which are dynamic, disordered, and difficult to characterize. Polycrystalline ice at ambient conditions offers several vivid examples of such environments. For instance, at temperatures above -10 °C, the whole concept of ice surface as a sharp interface between gas and solid phases becomes void due to the formation of an interfacial melting region, which may exceed hundreds of molecular diameters.^{1–3} Interfaces between ice and another solid, as

well as impurity rich grain boundaries in polycrystalline ice, may also become dynamic at temperatures approaching ice melting point.^{1–13} The exploration of such condensed phase systems began only recently, and the few available experimental results offer only a glimpse of their distinctiveness in terms of structure, physical properties, and reactivity. This stems from limitations in current experimental techniques typically used in the field of solid state chemistry.

The vaporization kinetics of water and various dopants, bulk and surface transport phenomena, and reactivity of ice have been investigated extensively over the past three decades using variants of high vacuum thermal desorption spectroscopy (TDS).^{12–23} In such experiments, thin ice films doped with various chemical species were grown on a flat substrate at cryogenic temperatures in vacuum. During preparation, the vaporization of the ice sample, diffusive transport of dopants, and reactions do not occur due to the low temperatures at which the films are deposited. The temperature is then raised in a controlled fashion, and chemical and physical phenomena in the films are monitored with a sensitive and selective analytical technique. The power of this approach arises, first, from the precise control of the film’s microstructure and, second, from the ability to apply a variety of analytical techniques to monitor properties of the thin films.^{12–23} Although TDS results provided the foundation for the understanding of the structure and reactivity of ice at cryogenic temperatures, it was not until recently that the method could be applied at temperatures above -40 °C due to the high volatility of this molecular solid.

The equilibrium vapor pressure of ice (4.6 Torr) implies a vaporization rate on the order of 10^6 – 10^7 ML/s at 0 °C. In addition to imposing a tremendous gas load on a pumping

^{a)} Author to whom correspondence should be addressed. Chemistry Department, The George Washington University, 21st St. NW, Room 107, Washington, D. C. 20052. Electronic mail: vlad@gwu.edu

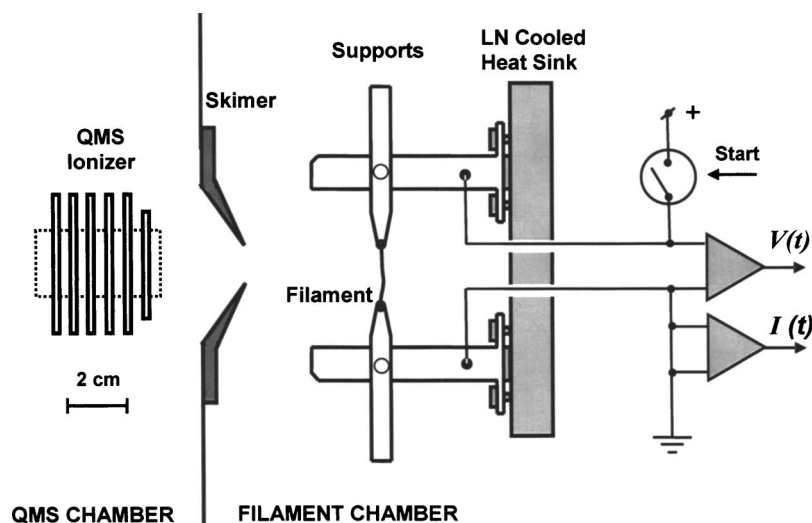


FIG. 1. Outline of the fast thermal desorption spectroscopy apparatus. The filament assembly consists of a tungsten filament spot welded to the supports. The supports are in thermal contact, but electrically isolated from a liquid nitrogen cooled heat sink. The vaporization flux from the filament is monitored with a quadrupole mass spectrometer (QMS) positioned in a differentially pumped vacuum chamber 10 cm from the filament. Vaporization products enter the QMS chamber through a 2 mm skimmer. During experiments, the voltage drop across the filament and the current through the filament are measured every 4 μ s.

system of any high vacuum TDS apparatus, the rapid vaporization of ice creates an array of practical problems, such as high thermal gradients across the sample, the formation of a boundary vapor layer above the ice surface, and the need for sample heating rates in excess of thousands of degrees per second.²⁴ With the objective of gaining fundamental insights into the phase transition, surface morphology, and transport phenomena in ice, we have developed a unique experimental approach, which allows us to overcome numerous challenges associated with the introduction of volatile materials into a high vacuum environment and makes it possible to study them with TDS at temperatures as high as 0 °C.²⁴

The core of our experimental apparatus is a thin (10 μ m in diameter) tungsten filament, which serves as a substrate for the vapor deposition of ice films at cryogenic temperatures. Following the deposition, the film is rapidly heated to a temperature near 0 °C by passing an electrical current through the filament. The microscopic dimensions of the ice films provide a number of crucial advantages. First, the small surface area of ice films grown on a thin wire results in a small net flux of desorbing molecules, which reduces the gas load on the vacuum system to manageable levels. Second, the small thermal mass of the thin wire facilitates heating rates in excess of 10^5 K/s, thus making it possible to bring the temperature of the ice film from cryogenic to ambient temperatures before a significant fraction of the film vaporizes. Third, the use of the thin wire as a substrate for ice deposition facilitates the calorimetric measurements of the ice mass because the total heat capacity of the ice sample is comparable to the total heat capacity of the substrate (filament). Finally, since the filament's diameter is near the mean free path of water molecules in saturated vapor at 0 °C, the formation of a boundary vapor layer around the filament is impossible.^{24,25} In summary, using a thin filament as the substrate for ice deposition makes it possible to extend the TDS approach to ambient temperatures. Due to the short time scales of our experiments we term our approach fast thermal desorption spectroscopy (FTDS).

Recently, we improved the design of our FTDS apparatus to include a sensitive quadrupole mass spectrometer

(QMS) positioned near the ice sample. Using this new arrangement, we conducted mass-selective studies on the vaporization kinetics of various chemical species from *doped* ice films. This article reports the results of our experiments with polycrystalline ice films, which contained thin H_2O^{18} tracer layers. By monitoring the vaporization flux of H_2O^{18} from ice films at various temperatures, we were able to distinguish between water vaporization kinetics of ice single crystals and those of various surface defects, characterize the variation in surface morphology of ice films undergoing rapid desorption, and gain insights into the diffusivity of water along the grain boundaries in the bulk of polycrystalline ice samples.

II. EXPERIMENT

A detailed description of the FTDS apparatus and standard experimental procedures can be found elsewhere,²⁴ therefore, only a brief description is provided in this section. As shown in Fig. 1, ice films are grown on the surface of a tungsten filament (10 μ m in diameter, 2 cm long), which is spot welded to the supports of the filament assembly. The supports, while in thermal contact with the liquid nitrogen cooled heat sink, are electrically isolated from the rest of the apparatus. The filament assembly includes a thermal control system capable of maintaining the filament supports at temperatures in a range from -160 to -120 °C. The assembly is surrounded by cryogenic shields and positioned in a vacuum chamber pumped with a 2500 s⁻¹ Varian diffusion pump. The cryogenic shields significantly reduce the gas load on the pumping system of the apparatus, allowing it to maintain pressures below 3×10^{-7} Torr during all stages of FTDS experiments.

Water vapor (H_2O^{16} and H_2O^{18}) is delivered from the vapor source to the filament via 12 effusive dosers made of 1/8 in. stainless steel tubes, which are equally spaced around the filament at a distance of approximately 5 cm from its center (not shown in Fig. 1). The intersecting vapor beams from the dosers leads to the formation of a relatively dense H_2O vapor cloud around the tungsten filament and, thus,

facilitates the deposition of uniform ice films with a neat cylindrical geometry and thickness of 0.1–4.0 μm over a period of a few minutes.

After deposition, rapid isothermal desorption of the film was initiated by applying a 2–5 V potential difference across the filament. In the course of the entire FTDS experiment, the voltage across the filament and the current through the filament were recorded every 4 μs by a custom designed data acquisition system. The effective resistance values were calculated from current and voltage data according to Ohm's law. The temperature was then calculated from the resistance data using the following equation:

$$T(R) = T_0 - (1/\alpha)(1 - R/R_0), \quad (1)$$

where α is the temperature coefficient of electrical resistivity of tungsten ($0.0045 \text{ }^\circ\text{C}^{-1}$) and R_0 is the value of the effective resistance of the filament at a known temperature T_0 . A calibration procedure, based on the melting of micrometer thick polycrystalline ice films, was routinely performed to ensure the $\pm 1.5 \text{ }^\circ\text{C}$ overall accuracy of filament temperature measurements.²⁴

The FTDS experiments are characterized by high heat fluxes through the ice films undergoing isothermal desorption at temperatures near melting point. This raises concerns about temperature gradients across the film bulk. In order to maintain a steady state isothermal vaporization of an ice film, the power generated by the filament must match the cooling of the filament by ice vaporization at a particular temperature. The efficiency of cooling by vaporization can be estimated as the product of ice vaporization enthalpy ($\sim 50 \text{ kJ/mol}$) and the maximum vaporization rate of ice, which gives 200 W cm^{-2} for the value of the heat flux across the ice film at $0 \text{ }^\circ\text{C}$.²⁴ Although this may seem high, such a heat flux does *not* necessarily result in large temperature gradients across a *thin* ice film. Assuming that the heat conductance of ice films is close to that of hexagonal ice ($2.2 \text{ W K}^{-1} \text{ m}^{-1}$), we obtain a temperature gradient of approximately $1 \text{ }^\circ\text{C } \mu\text{m}^{-1}$ for an ice film undergoing vaporization at $0 \text{ }^\circ\text{C}$.

Figure 2 provides further insights into isothermal vaporization process. It shows the H_2O flux from the filament and the corresponding temperature of the filament. The H_2O flux was measured with the fast ionization gauge (FIG), positioned 6 cm away from the filament behind the cryogenic shield.²⁴ Examination of the temperature data after 1.5 ms shows that the temperature of the filament is stable within $2 \text{ }^\circ\text{C}$. Achieving a steady state temperature coincides with the onset of H_2O desorption, which clearly follows zero-order kinetics for the next 5 ms. The observation of zero-order desorption kinetics leads to several important conclusions. First, during isothermal desorption near $0 \text{ }^\circ\text{C}$, the ice adlayer on the surface of the filament is a neat film free of *large* pores or ruptures, i.e., the film covers the entire filament surface.²⁴ Second, the temperature gradient *along* the length of the filament is negligible except within a fraction of a millimeter near the ends of the filament.²⁴ Finally, *since the temperature of the filament does not vary significantly with the film thickness during vaporization the temperature gradient in the film must be less than a few degrees.*²⁴

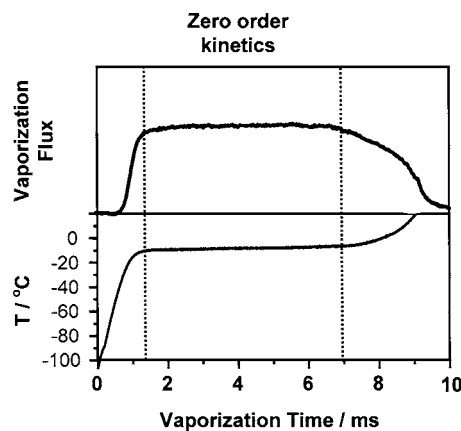


FIG. 2. H_2O flux from the filament and the corresponding temperature of the filament. The H_2O flux was measured with the fast ionization gauge (FIG), positioned 6 cm away from the filament. After 1.5 ms the temperature of the filament is stable within $2 \text{ }^\circ\text{C}$. Achieving a steady state temperature coincides with the onset of H_2O desorption, which follows zero-order kinetics for the next 5 ms.

In the past, we also used data from the time-of-flight (TOF) experiments to characterize thermal gradients across the bulk of vaporizing D_2O ice films.²⁴ In these experiments, the temperature of the ice *surface* was determined by fitting Maxwellian distributions to the experimental TOF spectra and was compared to the temperature of the filament derived from resistance measurements. The temperature values obtained by these two methods were equal within the experimental errors ($\pm 3 \text{ }^\circ\text{C}$), thus proving that the temperature gradients in FTDS experiments are indeed small.

The experiments described in this article rely on precise measurements of ice film thickness. The mass, thickness, and phase composition of our ice samples were determined by an ultrafast microcalorimetry technique.²⁴ In these experiments, the combined effective heat capacity of the ice film and the filament was calculated as the ratio of the power generated by the filament to the first time derivative of the temperature. Figure 3 illustrates typical results. The dashed line shows the effective heat capacity of the ice-free filament; the solid line shows the effective heat capacity of the filament with an H_2O film vapor deposited at $-120 \text{ }^\circ\text{C}$; and the dotted line shows the effective heat capacity of the filament with an H_2O film vapor deposited at $-150 \text{ }^\circ\text{C}$. In the case of deposition at $-120 \text{ }^\circ\text{C}$, the monotonic increase in heat capacity of the filament-film system, i.e., the lack of exothermic transitions characteristic of crystallization, demonstrates that the ice sample is crystalline. However, in the case of films deposited at $-150 \text{ }^\circ\text{C}$, the effective heat capacity of the film shows partially overlapping irreversible exotherms, which we attribute to crystallization of the initially amorphous ice samples.²⁴ The assignment of the exotherms shown in Fig. 3 to the crystallization of amorphous ice is facilitated by the 2 kJ/mol enthalpy release, which is close to previously reported values.^{25,26} These calorimetric experiments also show that noncrystalline ice films always undergo crystallization before steady state vaporization can occur at temperatures above $-25 \text{ }^\circ\text{C}$.

In addition to providing information on the phase composition of ice samples, the data shown in Fig. 3 were used

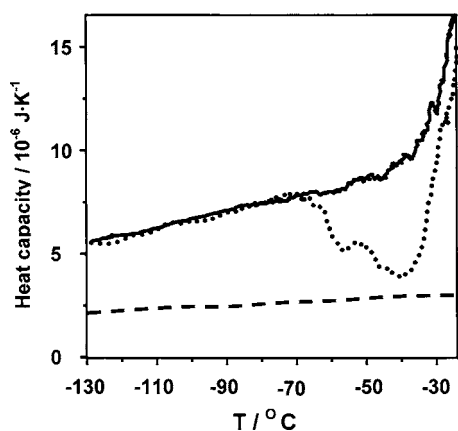


FIG. 3. Typical results of ultrafast microcalorimetry measurements. Dashed line: the effective heat capacity of the ice-free filament. Solid line: the effective heat capacity of the filament with an H_2O film vapor deposited at -120°C . Dotted line: the effective heat capacity of the filament with an H_2O film vapor deposited at -150°C . In the case of deposition at -120°C , the lack of exothermic transitions demonstrates that the ice sample is crystalline. In the case of films deposited at -150°C , the effective heat capacity of the film shows partially overlapping irreversible exotherms due to the crystallization of the initially amorphous ice samples.

to determine the masses of the ice films. Assuming that the film has the specific heat capacity and density of hexagonal ice, the estimate of the total mass of the film can be obtained by simply dividing the total heat capacity of ice film by the specific heat capacity of hexagonal ice. Using the mass of the ice film and assuming that ice film geometry is close to that of a neat cylinder, we routinely determine the thickness of our films with accuracy of $\pm 10\%$.

During FTDS experiments, the kinetics of the H_2O^{18} vaporization were monitored with a QMS. The QMS, a modified residual gas analyzer (RGA 300, Stanford Research Instruments), is positioned inside a small, differentially pumped vacuum chamber. The pumping system of the QMS chamber consists of 150 L s^{-1} turbo-molecular pump, which is backed with a diffusion pump. The pressure inside the QMS chamber is maintained at 10^{-8} Torr. Our QMS employs a specially designed electron bombardment ionizer, which is cooled with liquid nitrogen (LN). LN cooling significantly reduces the interference from condensable background gases. Vaporization products enter the QMS chamber through a 2 mm skimmer, which is situated 4 cm away from the filament. The distance from the filament to the ionizer is 10 cm.

In addition to serving as our primary detector for H_2O^{18} , the QMS was also used to check for the contamination of ice films with impurities. We emphasize that the contamination of our ice films with pump oil and other background gases is exceedingly low, despite the use of oil diffusion pumps to maintain a vacuum in the filament chamber. The low level of contaminants is due to the cryogenic shielding of the filament assembly, the relatively high temperature of ice deposition, and the short time scale of our experiments.²⁴

III. RESULTS AND DISCUSSION

A. Isothermal vaporization spectra of H_2O^{18}

Figure 4 illustrates typical results of a FTDS experiment with “sandwichlike” polycrystalline $\text{H}_2\text{O}^{16}/\text{H}_2\text{O}^{18}/\text{H}_2\text{O}^{16}$

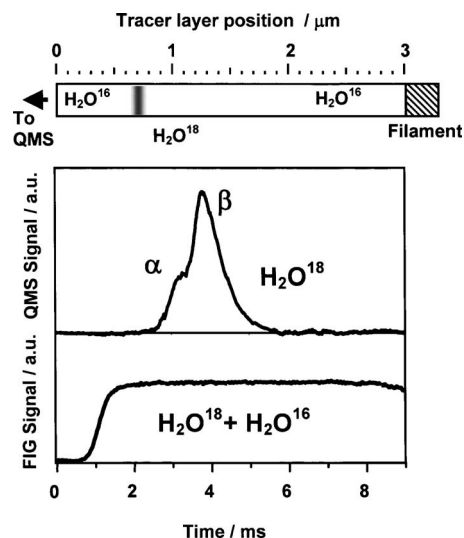


FIG. 4. FTDS spectrum of H_2O^{18} from a $3\ \mu\text{m}$ thick “sandwich-like” $\text{H}_2\text{O}^{16}/\text{H}_2\text{O}^{18}/\text{H}_2\text{O}^{16}$ film (upper panel). The H_2O^{18} tracer layer initially positioned approximately 700 nm under the film surface, as illustrated in the diagram on top the graph. The vaporization temperature was -8°C . Isothermal desorption kinetics of the entire ice film monitored by the FIG are shown for comparison (lower panel).

films. It compares the overall vaporization kinetics of the film (lower panel) and the vaporization kinetics of the H_2O^{18} isotopic tracer layer initially positioned at a depth of approximately 700 nm under the film’s surface (top panel). The film was prepared according to following procedure: First, a $2.5\ \mu\text{m}$ layer of H_2O^{16} was deposited on the surface of the filament over the time period of approximately 2 min. The film was then dosed with H_2O^{18} vapor for about 2 s. After the H_2O^{18} dosing, the filament was exposed to H_2O^{16} vapor for another 30 s. The deposition temperature was -120°C , which ensured the complete crystallization of the film, while minimizing low temperature vaporization and diffusion in the film. After the film deposition, a trigger pulse from the data acquisition system initiated the rapid heating and desorption of the film.

As shown in Fig. 4, the vaporization of the H_2O^{18} layer is significantly delayed as compared to the onset of ice desorption and consists of two distinct features: a shoulder at 3 ms and a peak at 4 ms. The delay in the vaporization of H_2O^{18} indicates that the transport of tracer molecules to the film’s surface is slow compared to the vaporization of the film. The delay in the vaporization of the H_2O^{18} layer supports our earlier conclusion that the ice film is free of large pores or ruptures and that it does not collapse into droplets or clusters until most of the film has been vaporized. Indeed, the rupturing of the film would create pathways for the rapid transport of tracer molecules toward the film’s surface, which is inconsistent with the observed delay in the vaporization of H_2O^{18} . Furthermore, the delay in the H_2O^{18} vaporization implies a relatively low self-diffusivity of water in polycrystalline ice during all of the stages of the FTDS experiment. Indeed, the H_2O^{18} desorption peak is delayed by 2 ms with respect to the onset of H_2O^{16} vaporization. Assuming that the $\text{H}_2\text{O}^{16}/\text{H}_2\text{O}^{18}/\text{H}_2\text{O}^{16}$ ice film desorbs with a constant rate equal to its maximum possible value of $0.33\text{ mg/cm}^2\text{ s}$

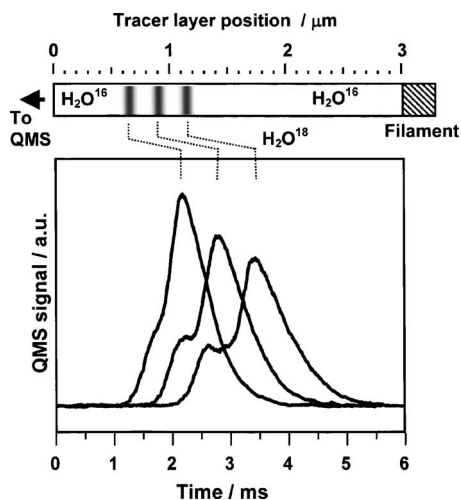


FIG. 5. Isothermal desorption spectra of H_2O^{18} from $3\ \mu\text{m}$ thick polycrystalline ice films at $-8\ ^\circ\text{C}$. The diagram on top of the graph shows the initial positions of the H_2O^{18} isotopic tracer layers.

($0.3\ \mu\text{m}$ of ice film thickness per second) at $-8\ ^\circ\text{C}$, a simple calculation gives $670\ \text{nm}$ for the thickness of the H_2O^{16} overlayer that needs to evaporate in order to release the H_2O^{18} tracer layer. This is in excellent agreement with $700 \pm 70\ \text{nm}$ thickness of the actual H_2O^{16} layer in the FTDS experiment, which is illustrated in Fig. 4. As we discuss later in this article, this is possible only if the effective diffusivity of H_2O^{18} is low compared to the vaporization of the film.

The most important characteristic of the H_2O^{18} isothermal desorption spectrum is the well pronounced shoulder preceding the main vaporization peak. The existence of two distinct features indicates that there are two different pathways for H_2O^{18} effusion from the ice film. Because ice films grown on a cylindrical substrate must be highly polycrystalline, the presence of distinct features in the isothermal desorption spectrum may be explained by the differences in the vaporization mechanisms for H_2O^{18} molecules initially trapped along grain boundaries and in the crystallites. Thus, the position, width, and intensity of H_2O^{18} desorption peaks may carry information on the microscopic structure of the ice films and may, in principle, be used to estimate many important physical parameters, such as water self-diffusivity along the grain boundaries. In order to facilitate a quantitative analysis of the transport phenomena and morphological dynamics in polycrystalline ice, we have obtained a series of isothermal desorption spectra for the films in which the initial position of the tracer layer and the desorption temperature were varied in a systematic fashion. The representative results of these experiments are shown in Figs. 5 and 6.

Figure 5 shows selected isothermal desorption spectra of thin H_2O^{18} layers from $3\ \mu\text{m}$ thick polycrystalline H_2O^{16} ice films. While the overall dimensions of the films were identical in each experiment, the initial position of the tracer layer, with respect to the surface, varied from 450 to $1550\ \text{nm}$. As shown in the figure, positioning the tracer layer further away from the film's surface resulted in *near-linear* shifts in the α and β features of the H_2O^{18} desorption spectra. Moreover, the change in the position of the main peak is typically greater than that in the position of the shoulder. This leads to

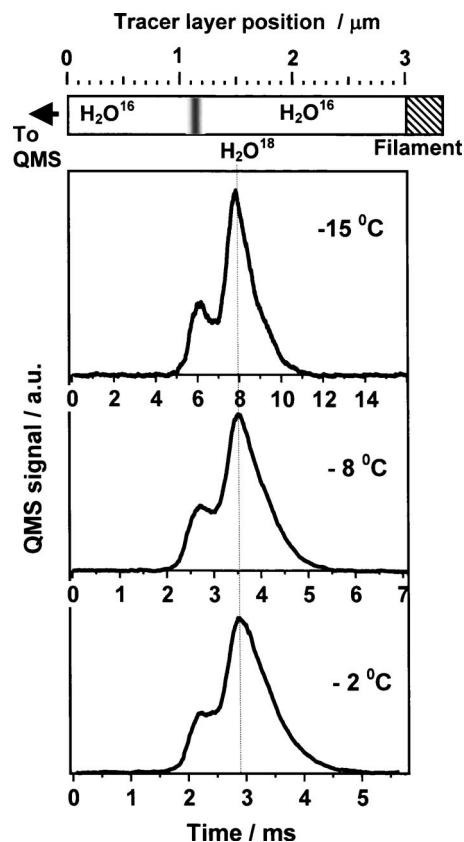


FIG. 6. Isothermal desorption spectra of H_2O^{18} from $3\ \mu\text{m}$ thick polycrystalline ice films measured at various temperatures. The diagram on top of the graph shows the initial positions of the H_2O^{18} isotopic tracer layers.

a greater separation of the two features in the thermal desorption spectra, as the tracer layers are buried deeper into the bulk of the ice films.

Figure 6 illustrates the dependence of the H_2O^{18} isothermal desorption spectra on the steady state temperature. In these experiments H_2O^{18} layers were always positioned $1150\ \text{nm}$ away from the surface of $3\ \mu\text{m}$ thick films. While the dimensions of the film remained the same, the steady state vaporization temperature of the film was varied. The upper, middle, and lower panels of Fig. 6 show isothermal desorption spectra of ice films of identical structure and geometry measured at -15 , -8 , and $-2\ ^\circ\text{C}$, respectively. In order to facilitate a qualitative comparison of these spectra, the desorption time was scaled so that the positions of the main peak (β feature) would visibly coincide.

As shown in Fig. 6 the overall shapes of the desorption spectra measured at various temperatures are nearly identical. A slight smoothing of the features in the spectrum shown in the lower panel, measured at $-2\ ^\circ\text{C}$, may be explained by the variations in the time of flight of H_2O^{18} molecules traveling across a $10\ \text{cm}$ distance, which separates the filament from the QMS detector. Indeed, an infinitely short burst of H_2O molecules from the filament surface at $0\ ^\circ\text{C}$ would be recorded as an approximate $200\ \mu\text{s}$ wide Maxwellian TOF distribution by a detector positioned $10\ \text{cm}$ away from the source. Since the overall isothermal desorption time for H_2O^{18} at temperatures near $0\ ^\circ\text{C}$ is significantly shorter than that at $-15\ ^\circ\text{C}$ (see Fig. 6), the TOF broadening must have a

greater effect on the spectra measured at higher temperatures. Taking into account the small contribution of TOF broadening in the isothermal desorption spectra in Fig. 6, we arrive at this important conclusion: the isothermal desorption spectra of H_2O tracer layers, measured at various temperatures, scales linearly with time. In other words, the vaporization rate of H_2O^{18} [$\mathcal{R}(T_{\text{des}}, t)$] has the following property:

$$\mathcal{R}(T_{\text{des}1}, t) = \mathcal{R}(T_{\text{des}2}, \chi t) \quad (2)$$

where T_{des} is the isothermal desorption temperature, t is the desorption time, and χ is a numeric factor.

In order to elucidate the details of the H_2O^{18} vaporization from H_2O^{16} ice films, we have collected a large number of isothermal desorption spectra of tracer layers initially positioned at various distances from the film surface. The measurements were conducted at -2 , -5 , -8 , and -15 °C. The total thickness of the ice film in all experiments was approximately three micrometers. As we will show in the following sections, these data make it possible to distinguish between the vaporization kinetics of water from single crystals and those from grain boundaries of our polycrystalline ice films and to obtain insights into film's morphology.

B. H_2O^{18} vaporization mechanisms

We begin by emphasizing that the observation of distinct structures in the isothermal spectra *cannot* be explained by diffusion of H_2O^{18} through the ice films during deposition. This conclusion comes from experiments in which the deposition temperature of ice was varied from -155 to -115 °C. In spite of significant variations in the deposition temperature, the H_2O^{18} spectra are virtually independent of ice deposition conditions. Furthermore, delaying the desorption experiment by several minutes following the deposition did not result in any noticeable changes in the H_2O^{18} spectra. Since the initial morphology of the film and, consequently, the diffusive transport of tracer molecules depends on the preparative conditions, the lack of observable changes demonstrates that characteristic features of the H_2O^{18} spectra are not determined by low temperature transport phenomena.

As we have already mentioned, the two features in the isothermal desorption spectra of the tracer layer indicate two distinct pathways for H_2O^{18} effusion from the film near ambient temperatures. Taking into account the polycrystallinity of our ice samples, we assign the “fast” α component of the spectrum to H_2O^{18} vaporization facilitated by the grain boundaries and related defects and the “slow” β component to the vaporization of H_2O^{18} molecules trapped in the interior of the crystallites. In order to validate these assignments, we conducted isothermal desorption experiments with sandwichlike $\text{H}_2\text{O}^{16}/\text{H}_2\text{O}^{18}/\text{H}_2\text{O}^{16}$ films, which were also uniformly doped with acetic acid. The mole fraction of CH_3COOH was relatively small (0.1) and did not affect the overall desorption kinetics of the film.

The addition of CH_3COOH molecules to the ice sample resulted in significant changes (broadening and an increase in the relative magnitude) in the α feature of the H_2O^{18} desorption spectrum, as shown in Fig. 7. Nevertheless, the position and width of the β peak remained unaffected. Since

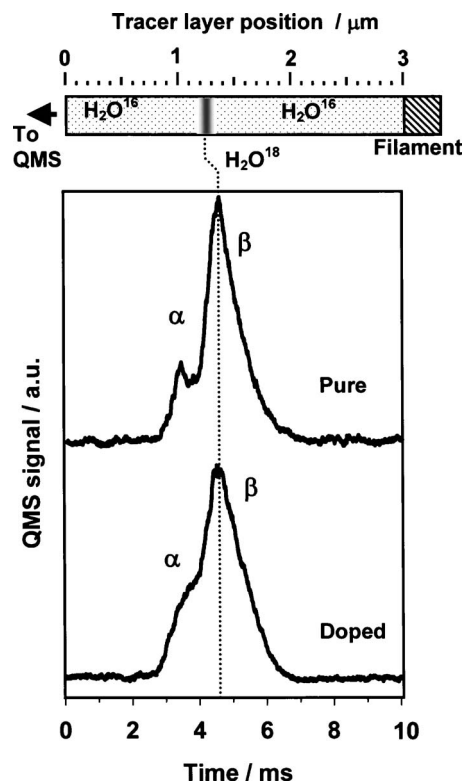


FIG. 7. Isothermal desorption spectrum of H_2O^{18} from $3 \mu\text{m}$ thick pure polycrystalline ice films and from films uniformly doped with acetic acid. The mole fraction of CH_3COOH was 0.01. The overall vaporization rate of doped ice was indistinguishable from that of pure ice. The diagram on top of the graph shows the initial positions of the H_2O^{18} isotopic tracer layers. The addition of acetic acid results in significant changes in the α feature; however, the position and width of the β feature remains unaffected.

dopants incompatible with the crystalline structure of a pure solid tend to aggregate at the grain boundaries in polycrystalline materials,^{28–38} the lack of changes in the β feature but significant changes in the α feature validates our assignment of the vaporization peaks. Indeed, the addition of acetic acid to polycrystalline ice is likely to result in a smaller average size of the crystallites and, consequently, in a higher density of the grain boundaries and related defects due to the solvent drag on the grain growth.^{39–42} Furthermore, concentrated impurities may change the H_2O^{18} diffusivity along the grain boundaries, while the diffusivity of H_2O^{18} trapped in relatively pure crystallites is likely to remain the same. Variations in the α feature and the lack of variations in the β part of the spectrum are consistent with the assignment of the α peak to the H_2O^{18} vaporization channel facilitated by the grain boundaries and the β feature to the vaporization of H_2O^{18} trapped in the crystallites.

Having identified the general nature of the α and β peaks, we can now attempt to infer details of the processes which give rise to a distinct structure of the isothermal desorption spectra of H_2O^{18} . Since the vaporization of the H_2O^{18} tracer layer involves two major steps (i.e., diffusion toward the film's surface and the subsequent desorption), there are two possible scenarios which may explain the double-peak structure of the H_2O^{18} spectrum. The first scenario, illustrated in Fig. 8(a), assumes that the changes in the film's surface morphology, during isothermal vaporization,

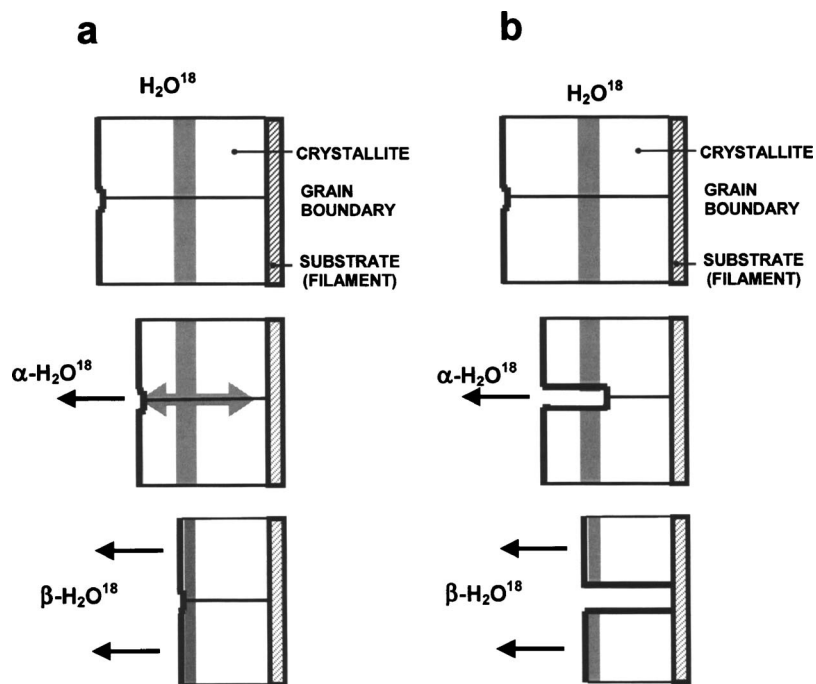


FIG. 8. Two possible mechanisms of H_2O^{18} vaporization. (a) The case where the changes in the ice film's surface morphology are assumed to be negligible; whereas, the diffusion of H_2O^{18} along the grain boundaries is rapid. Rapid diffusive transport of isotopic tracer molecules to the film's surface results in the α peak. The subsequent β peak arises from desorption of the H_2O^{18} molecules trapped in ice crystallites. (b) The case where the diffusion of the tracer species within the film's bulk is negligible but the surface undergoes thermal etching during vaporization. Isotopic tracer species located at or near the grain boundaries vaporize, when grooves and pits reach the tracer layer, thus resulting in the α peak in the desorption spectra of H_2O^{18} . The β peak signifies desorption of the H_2O^{18} molecules trapped in ice crystallites.

are negligible; whereas, the diffusion of H_2O^{18} along grain boundaries is rapid. As illustrated in the figure, the rapid diffusive transport of isotopic tracer species toward the surface of the film results in the early α peak, which is then followed by the β peak due to vaporization of H_2O^{18} trapped in the crystallites. The feasibility of this vaporization mechanism is supported by our Monte Carlo simulations of the diffusion-desorption process, which show that rapidly diffusing molecules emerge from the film at an earlier time.

The alternative explanation of the H_2O^{18} desorption spectra is illustrated in Fig. 8(b). This hypothesis assumes that the diffusion of the tracer species in the film's bulk is negligible on the time scale of the desorption experiment, while the vaporization is accompanied by rapid changes in the *surface morphology* of the film. As shown in Fig. 8(b), the vaporization of water molecules from the grain boundaries and related defects may lead to pitting or grooving of the film. Thus, channels growing from the film's surface toward the substrate provide a path for the vaporization of tracer molecules initially situated at or near the grain boundaries and give rise to an α peak in the isothermal vaporization spectrum of H_2O^{18} . The α peak is followed by a β peak, due to the release of H_2O^{18} molecules trapped in the interior of the crystallites, which vaporize at a slower rate compared to defect rich grain boundary regions of the film. In the following section, we provide the arguments, which make it possible to differentiate between these two mechanisms.

C. Morphological dynamics versus diffusive transport

In order to distinguish between the two vaporization mechanisms depicted in Fig. 8, we have conducted a careful analysis of H_2O^{18} vaporization spectra measured under various conditions. Furthermore, we have also compared vaporization spectra of H_2O^{18} tracer layers with those of HDO. Immediately below, we provide several arguments against the diffusion based mechanism of tracer vaporization.

First of all, the isothermal desorption spectra of HDO appear to be indistinguishable from those in the case of H_2O^{18} . Taking into account the fact that diffusion rates of HDO in ice may differ significantly from those of H_2O^{18} ,¹⁹ the observed lack of distinctions between HDO and H_2O^{18} spectra is inconsistent with the diffusion based mechanism.

Second, as shown in Fig. 5, the vaporization spectra of H_2O^{18} from identical films at various steady state temperatures scale linearly with time. Because the vaporization kinetics of a tracer layer buried in the bulk of an ice film are determined by a convolution of at least two processes (i.e., the diffusion of the tracer species in the bulk of the film and their consequent desorption from the film's surface), the vaporization spectra depend on at least two physical parameters. These are the isothermal vaporization rate of H_2O^{16} ice initially covering the tracer layer and the diffusivity of H_2O^{18} in H_2O^{16} ice,

$$\mathcal{R}_{H_2O^{18}}(T, t) = \mathcal{F}\{\mathcal{R}_{H_2O^{16}}(T), \mathcal{D}_{H_2O^{18}}(T)\}. \quad (3)$$

Both of the parameters, the H_2O^{16} vaporization rate and the H_2O^{18} diffusivity, must have strong and distinct dependences on temperature. Assuming that both processes contribute significantly to the overall vaporization kinetics and taking into account the convolution of the diffusive transport and surface desorption of H_2O^{18} , it is extremely unlikely that the resulting vaporization spectra measured at various steady state temperatures would follow a simple time scaling law. However, if we assume that the contribution of the diffusive transport is negligible (i.e., that H_2O^{18} molecules are nearly immobilized in the bulk of the ice film until they are released into the gas phase by the vaporization of the H_2O^{16} overlayer), the vaporization rate of the tracer species may be represented as a simple product of the steady state vaporization rate of H_2O^{16} ice and the initial concentration profile of the H_2O^{18} .²⁰ Since the vaporization rate of H_2O^{16} ice is nearly constant at a particular steady state temperature, the

resulting H_2O^{18} desorption spectra of *identical* tracer layers measured at various temperatures would, then, scale linearly with time. Thus, the linear time scaling of H_2O^{18} spectra measured at various temperatures provides further basis for the rebuttal of the diffusion based vaporization mechanism.

Finally, careful examination of the data in Fig. 4 shows that the slope of the leading edge of the α feature in the vaporization spectra of H_2O^{18} does not depend on the initial position of the tracer layers in the ice film. This may be interpreted as a lack of desorption spectrum broadening for the H_2O^{18} layer initially positioned deep in the bulk of the H_2O^{16} ice film. However, broadening, and consequently the decrease in the slope of the leading edge of the spectra of tracer layers positioned deeper in the bulk of the film, is expected in the case of rapid diffusion of the tracer species. According to our Monte Carlo simulation, such a broadening must be apparent if the effective diffusion coefficient for H_2O^{18} is greater than $10^{-3} \mu\text{m}^2 \text{s}^{-1}$. The broadening of the spectra is a direct consequence of the increase in the variance of the dopant concentration profile with time, which is predicted and observed for virtually any type of random diffusive process.^{43–46} Therefore, the lack of significant variations in the leading slope of the α peak supports our conclusion that the contribution of the bulk diffusive transport of H_2O^{18} to the overall vaporization kinetics of the tracer is insignificant.

Whenever the diffusion based mechanism of the H_2O^{18} vaporization fails to agree with the experimental data, the spectrum interpretation based on the possible variations in the ice surface morphology provides a ready explanation. For example, assuming that the α and β features in the tracer layer spectra are due to a difference in the vaporization rates from defect-rich and defect-free parts of the ice film's surface, the vaporization spectra of HDO and H_2O^{18} must show absolutely no distinctions because, in the limit of low diffusion, the overall kinetics are determined by the vaporization kinetics of the H_2O^{16} *overlayer*. The only experimental observation, which may seem to be inconsistent with the H_2O^{18} vaporization mechanism shown in Fig. 8(b), is the apparent overall zero-order desorption kinetics of the film (see Fig. 4).

It is true that the formation of the pores or channels in the film must lead to a gradual increase in the overall surface area of the film and, thus, to non-zero-order vaporization kinetics. We emphasize, however, that the extent of deviation from the zero-order vaporization kinetics must depend on the geometry and dimensions of the pits and grooves on the polycrystalline ice surface. For example, 1 nm wide grain boundary grooves around crystallites with effective radii on the order of a few *hundred* nanometers will occupy a relatively small fraction of the total surface area of the film, thus making the variations in the total effective area of the film hard to detect. Furthermore, if the thermal grooving of the ice surface produces nanometer wide channels that are relatively narrow and deep, water molecules desorbing from the walls of the grooves will not be able to escape immediately into the gas phase. Therefore, in spite of the microscopic channels in the bulk of the ice film, the total surface area available for the *free* vaporization of water molecules may

remain constant making near zero-order vaporization kinetics possible.

Taking into account the specific conditions present in our experiments (i.e., temperatures near ice melting point and rapid vaporization), an etching of the surface of the ice films illustrated in Fig. 8(b) is not surprising. Thermal grooving and pitting of the surface are well known phenomena observed in experiments with a variety of polycrystalline materials.^{47–50} Even at temperatures significantly below melting point, a thin film of a polycrystalline material will eventually collapse into separated crystallites on a nonwetting substrate by the formation of gradually deepening grooves on the sample's surface.^{51–54} In the case of polycrystalline ice near melting point, this process may be sufficiently rapid so that it will be manifested on the time scale of our tracer vaporization experiment. Indeed, thin ice films do not wet most surfaces and are inherently unstable.⁵⁵ Thus, during rapid vaporization, etching of the film along the grain boundaries and related defects is expected. While the formation of the grain boundary grooves may not significantly change the overall vaporization kinetics of ice samples, according to our results, it certainly provides an effective pathway toward the surface for the tracer species trapped in the film's bulk.

D. Vaporization rate of water from ice single crystals

In the previous section of this article we demonstrated that the contribution of the bulk diffusion to the overall vaporization kinetics of H_2O^{18} tracer molecules from H_2O^{16} ice is negligible. In other words, we show that a thin H_2O^{18} tracer layer, initially positioned at a distance of several hundred nanometers under the surface of an ice film, evolves into the gas phase only when the H_2O^{16} overlayer has vaporized. Furthermore, the isothermal desorption spectra of H_2O^{18} show two distinct peaks, which are due to a difference between the vaporization of H_2O^{16} from ice single crystals and from the grain boundaries.

The low diffusivity of isotopic tracer species and the presence of a structure in the isothermal desorption spectra open a unique way for precise measurements of the absolute vaporization rates of H_2O^{16} from ice *single crystals*. Indeed, the thinning of the polycrystalline ice film by zero-order vaporization can be viewed as the motion of its free surface toward the substrate (filament). Thus, the initial position of a tracer layer in the bulk of the film can be used as a reference point for the position of the free surface of the film at the time of tracer desorption. By simply plotting the initial positions of the tracer layer as a function of the H_2O^{18} vaporization time, the “velocity” of film's free surface (i.e., the film's vaporization rate) can be determined with high accuracy. Assuming that distinct features in the vaporization spectrum of H_2O^{18} are due to unequal vaporization rates of H_2O^{16} from single crystals and grain boundary grooves, the vaporization rate from the grains and the grooves can be measured independently. For example, if the tracer layer is initially 1000 nm away from the surface, the position of the β peak in the isothermal spectrum gives the time required for the vaporization of 1000 nm thick ice single crystals. At the same

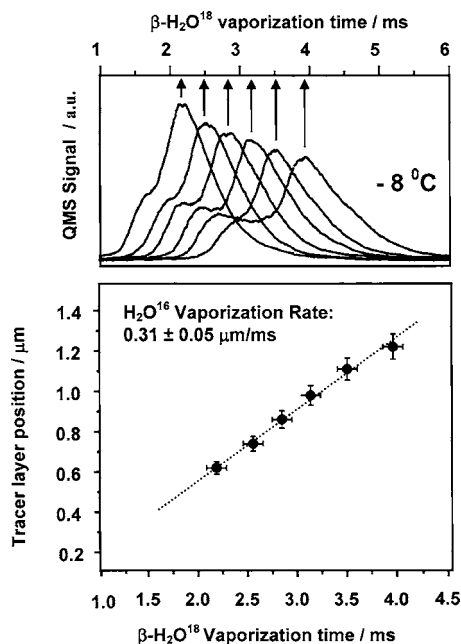


FIG. 9. Isothermal desorption spectra of H₂O¹⁸ from 3 μm thick polycrystalline ice films at -8 °C and plot of the initial tracer layer position as a function of vaporization time of β-H₂O¹⁸. According to the interpretation of the spectra described in the text, the slope of the line gives the vaporization rate of the single crystal part of the polycrystalline film.

time, the position of the α peak gives the characteristic time required for the vaporization of 1000 nm thick, disordered, aqueous phase from the grain boundary grooves.

Figure 9 illustrates our approach to H₂O¹⁶ vaporization rate measurements from ice single crystals. It shows the initial position of tracer layers as a function of the H₂O¹⁸ vaporization time, which is determined from the positions of the β peaks in the isothermal desorption spectra at -8 °C (top panel of Fig. 9). According to the interpretation of the spectra, the data depicted in the lower panel of Fig. 9 represents the thickness of the vaporized single crystal layer as a function of vaporization time. Thus, the slope of the linear fit to the data gives the absolute vaporization rate of H₂O¹⁶ from the ice single crystals in the units of μm/ms. As shown in the figure, the vaporization rate of single crystal ice is 0.31 ± 0.5 μm/ms, or about 900 000 ice monolayers per second at -8 °C.

Figure 10 summarizes the results of the desorption rate measurements of single crystal H₂O¹⁶ ice at various temperatures between -2 and -15 °C (black circles). Each rate value was obtained from the analysis of the H₂O¹⁸ vaporization spectra, as illustrated in Fig. 9. The dashed line in Fig. 10 shows the vaporization rate values calculated from the ice equilibrium vapor pressure, under the assumption that the mass accommodation coefficient of H₂O on ice is equal to unity.⁵⁶⁻⁵⁹ The gray circles represent the vaporization rate values for H₂O¹⁶ from *polycrystalline* ice, which were measured with a fast ionization gauge in our past experiments.²⁴ As shown in the figure, the vaporization rate of ice single crystals, within the errors of measurements, coincides with the vaporization rate of polycrystalline films and is near the maximum vaporization rate calculated from the vapor pressures values.

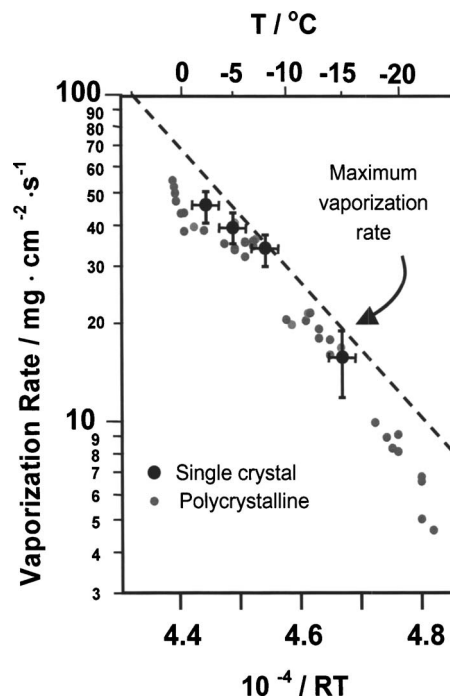


FIG. 10. Absolute vaporization rate of single crystal ice (dark circles), absolute vaporization rate of polycrystalline ice (grey circles), and the maximum vaporization rate (line) of ice as function of temperature.

In the past, we used measurements of the vaporization rate of polycrystalline ice to argue that the mobile precursor (MP) mechanism fails to describe the vaporization kinetics of ice near its melting point. Because the MP mechanism considers an idealized surface of ice single crystal, the vaporization rate measurements reported in Fig. 10, i.e., measurements of vaporization rate of water from *monocrystalline* parts of our ice samples, confirm and strengthen our arguments. The discrepancy between the predicted and measured rate values is apparent, when the comparison is done in terms of vaporization coefficient α_v which is defined as the ratio of the observed desorption rate to the maximum equilibrium desorption rate at a particular temperature,

$$\alpha_v(T) = \frac{J_v(T)}{J_{\max}(T)} = \frac{J_v(T)(2\pi mkT)^{1/2}}{P_{\text{ice}}(T)}, \quad (4)$$

where $P_{\text{ice}}(T)$ is the equilibrium vapor pressure of ice and $J_v(T)$ is the measured absolute vaporization rate.²⁴ Figure 11 shows the range of possible values of the vaporization coefficient for ice single crystals derived from the data in Fig. 10. Dimensions of the shaded field in the upper part of the Fig. 11 represent the overall accuracy of our α_v measurements. The shaded region shown in the lower part of Fig. 11 represents the range of vaporization coefficient values predicted by the MP mechanism.¹⁴ As shown in the figure, the experimentally determined vaporization coefficient for single crystal ice demonstrates only a weak dependence on temperature with values close to unity in the entire temperature range studied. In the past, we have argued that the failure of the MP mechanism to describe the vaporization kinetics of ice near its melting point is likely due to a surface disordering or premelting transition, which may occur at temperatures as low as -70 °C.^{6,7,10,60,61} The vaporization rate data reported

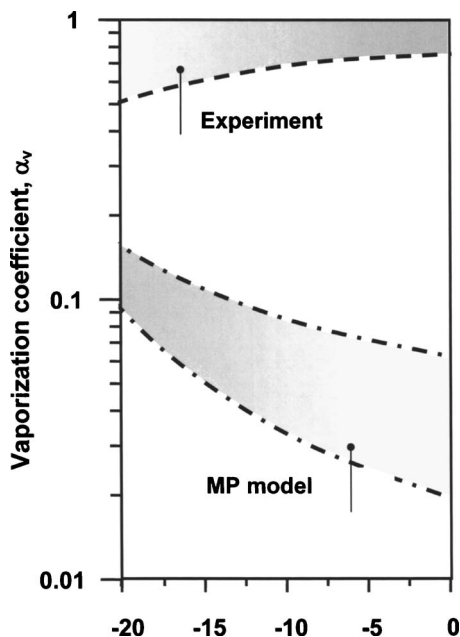


FIG. 11. Upper shaded region: The range of values of the vaporization coefficient derived from experimental measurements of the absolute vaporization rate of single crystal ice. The shaded region in the middle of the plot shows the range of values for vaporization coefficient predicted by the classical mobile precursor mechanism.

in this section prove that such a disordering transition would not be specific only for polycrystalline samples but also for ice single crystals.

E. Rate of surface etching

In the previous section of this article, we used the position of the β peaks in the isothermal desorption spectra of H_2O^{18} in order to determine the vaporization rate for ice single crystals. Using a similar analysis, we can determine the rate of surface etching along the grain boundaries of polycrystalline ice. Assuming that the α peak is due to the release of H_2O^{18} trapped at or near the grain boundaries and the β peak is due to the release of H_2O^{18} trapped in the crystallites, the average groove depth at the moment of α - H_2O^{18} release can be calculated using the following equation:

$$\text{Groove Depth} = R_{\text{cr}}(T)(t_{\beta} - t_{\alpha}), \quad (5)$$

where $R_{\text{cr}}(T)$ is the vaporization rate of crystallites, t_{β} is the moment of β - H_2O^{18} release (the position of the β peak), and t_{α} is the moment of α - H_2O^{18} release (the position of the α peak). Since t_{α} is a function of the initial position of the tracer layer, repeating these calculations for spectra with H_2O^{18} tracer layers initially situated at various distances from the film's surface makes it possible to determine the average depth of the pits and grooves at any time during vaporization.

Figure 12 shows the average depth of the surface grooves as a function of vaporization time for ice films desorbing at -2 , -8 , and -15 °C. At each temperature, the depth of the grooves on the surface of a polycrystalline ice film demonstrates a near-linear dependence with time. The effective rate of surface etching, determined from the linear fit of

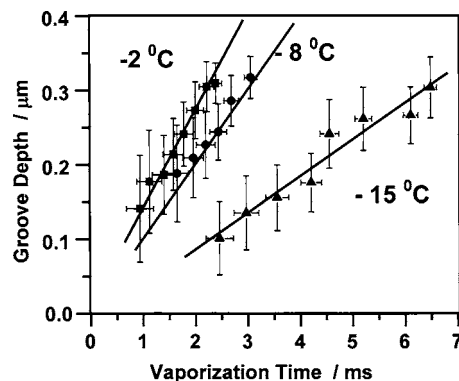


FIG. 12. The average depth of the surface grooves as a function of vaporization time, during vaporization of $3 \mu\text{m}$ ice films at various temperatures. The slopes of the lines give the rate of thermal etching of the polycrystalline surface.

data in Fig. 12, increases with temperature. At -15 , -8 , and -2 °C the etching rates are 0.05 , 0.09 , and $0.12 \mu\text{m}/\text{ms}$, respectively. Although the etching of the surface of polycrystalline ice during rapid vaporization is strongly manifested in the desorption spectra of H_2O^{18} isotopic tracer layers, the depth of the grooves is relatively small. For example, at -2 °C the deepening of the surface grooves occurs with the rate of about $0.12 \mu\text{m}/\text{ms}$, while the vaporization of the film takes place with the rate of approximately $0.45 \mu\text{m}/\text{ms}$, almost four times faster. The etching of the surface ultimately leads to the collapse of the film in the later stages of vaporization into droplets or clusters. As we already mentioned, this is evident from the overall vaporization kinetics shown in Fig. 2, which indicate that the last 20% of the ice film vaporizes with non-zero-order desorption kinetics. These observations emphasize the inherent instability of ice on various substrates observed in a variety of experiments.⁵⁵

IV. SUMMARY AND CONCLUSIONS

Using fast thermal desorption spectroscopy techniques, we have conducted the first measurements on the free vaporization rate of ice *single crystals* at temperatures near 0 °C. Our results show that single crystal ice vaporizes with rate significantly higher than previously thought. In contrast with some theoretical predictions, the vaporization coefficient of single crystal ice is above 0.5 for the entire temperature range studied and shows only a weak dependence on temperature. These measurements support and strengthen the conclusions of our previous work and show that the MP mechanism fails to describe the vaporization kinetics of ice single crystals at temperatures near ambient.

The tracer layer experiments indicate that the diffusive transport of H_2O^{18} molecules in the bulk of polycrystalline ice films is exceedingly slow compared to the vaporization of H_2O^{16} ice. Also, the polycrystalline ice films undergo thermal etching along the grain boundaries with the rate of 50 – $150 \text{ nm}/\text{ms}$ during rapid vaporization at temperatures near 0 °C.

Finally, our experiments demonstrate the power of the fast thermal desorption spectroscopy approach. Indeed, we show that by using FTDS it is possible to distinguish be-

tween the physical and chemical phenomena that occur along the grain boundaries and in the single crystals of polycrystalline ice at temperatures near its melting point and, thus, open new exciting opportunities for experimental research on these challenging condensed phase systems.

ACKNOWLEDGMENTS

The authors would like to thank William Rutkowski at the George Washington University Machine Shop for his engineering expertise during the design and fabrication of our research apparatus. We would also like to thank machinist Carl Behnke for the fabrication of various parts of our apparatus and Brandy Palmore, who contributed to data gathering. This work was supported by GW University Facilitating Fund and NSF Grant No.0416091.

- ¹J. G. Dash, in *Ice Physics and the Natural Environment*, NATO Advanced Studies Institute, Series I: Global Environmental Change Vol.: 56, edited by J. S. Wettlaufer, J. G. Dash, and N. Untersteiner (Springer, New York, 1999), pp. 11–22.
- ²J. S. Wettlaufer, *Philos. Trans. R. Soc. London, Ser. A* **357**, 1 (1999).
- ³H. Bluhm, D. F. Ogletree, C. S. Fadley, M. Salmeron, and Z. Hussain, *J. Phys.: Condens. Matter* **14**, L227 (2002).
- ⁴V. F. Petrenko and R. W. Whitworth, *Physics of Ice* (Oxford University Press, Oxford, 1999).
- ⁵J. S. Wettlaufer, *Phys. Rev. Lett.* **82**, 2516 (1999).
- ⁶I. Golecki and C. Jaccard, *J. Phys. C* **11**, 4229 (1978).
- ⁷D. Beaglehole and D. Nason, *Surf. Sci.* **96**, 357 (1980).
- ⁸Y. Furukawa and H. Nada, *J. Phys. Chem. B* **101**, 6167 (1997).
- ⁹V. Sadtchenko and G. E. Ewing, *J. Chem. Phys.* **116**, 4686 (2002).
- ¹⁰W. Xing, P. B. Miranda, C. Zhang, and Y. R. Shen, *Phys. Rev. B* **66**, 85401 (2002).
- ¹¹J. S. Wettlaufer, *Interface Sci.* **9**, 115 (2001).
- ¹²F. E. Livingston and S. M. George, *J. Phys. Chem. A* **102**, 10280 (1998).
- ¹³R. S. Smith, C. Huang, E. K. L. Wong, and B. D. Kay, *Phys. Rev. Lett.* **79**, 909 (1997).
- ¹⁴J. Gordon Davy and G. A. Somorjai, *J. Chem. Phys.* **55**, 3624 (1971).
- ¹⁵D. R. Haynes, N. J. Tro, and S. M. George, *J. Phys. Chem.* **96**, 8502 (1992).
- ¹⁶N. J. Sack and R. A. Baragiola, *Phys. Rev. B* **48**, 9973 (1993).
- ¹⁷D. E. Brown, S. M. George, C. Huang, E. K. L. Wong, K. B. Rider, R. S. Smith, and B. D. Kay, *J. Phys. Chem.* **100**, 4988 (1996).
- ¹⁸R. J. Speedy, P. G. Debenedetti, R. S. Smith, C. Huang, and B. D. Kay, *J. Chem. Phys.* **105**, 240 (1996).
- ¹⁹J. A. Smith, F. E. Livingston, and S. M. George, *J. Phys. Chem. B* **107**, 3871 (2003).
- ²⁰V. Sadtchenko, W. R. Gentry, and C. Giese, *J. Phys. Chem. B* **104**, 9421 (2000).
- ²¹J. D. Graham and J. T. Roberts, *J. Phys. Chem.* **98**, 5974 (1994).
- ²²A. Bar-Nun, I. Kleinfeld, and E. Kochavi, *Phys. Rev. B* **38**, 7749 (1988).
- ²³S. Haq, J. Harnett, and A. Hodgson, *J. Phys. Chem. B* **106**, 3950 (2002).
- ²⁴V. Sadtchenko, M. Brindza, M. Chonde, B. Palmore, and R. Eom, *J. Chem. Phys.* **121**, 11980 (2004).
- ²⁵M. Faubel, in *Photoionization and Photodetachment*, Advanced Series in Physical Chemistry Vol. 10A, edited by C.-Y. Ng (World Scientific, River Edge, NJ, 2000), Pt. 1, pp. 634–690.
- ²⁶For review, see R. A. Baragiola, in *Water in Confining Geometries*, Springer Series in Cluster Physics Vol. XII, edited by V. Buch and J. P. Devlin (Springer, Berlin, 2003), pp. 359–395.
- ²⁷Y. P. Handa, O. Mishima, and E. Whalley, *J. Chem. Phys.* **84**, 2766 (1986).
- ²⁸R. Mulvaney, E. W. Wolff, and K. Oates, *Nature (London)* **331**, 247 (1988).
- ²⁹E. W. Wolff, W. D. Miners, J. C. Moore, and J. G. Paren, *J. Phys. Chem. B* **101**, 6090 (1997).
- ³⁰H. Fukazawa, K. Sugiyama, S. Mae, H. Narita, and T. Hondoh, *Geophys. Res. Lett.* **25**, 2845 (1998).
- ³¹D. Cullen and I. Baker, *Microsc. Res. Tech.* **55**, 198 (2001).
- ³²D. Cullen and I. Baker, *J. Glaciol.* **46**, 703 (2000).
- ³³I. Baker and D. Cullen, *Ann. Glaciol.* **35**, 224 (2003).
- ³⁴D. Cullen, Ph.D. thesis, Dartmouth College, 2002.
- ³⁵J. Jouzel, J. R. Petit, R. Souchez, N. L. Barkov, V. Ya. Lipenkov, D. Raynaud, M. Stievenard, N. I. Vassiliev, V. Verbeke, and F. Vimeux, *Science* **286**, 2138 (1999).
- ³⁶D. Cullen and I. Baker, *Mater. Charact.* **5498**, 263 (2002).
- ³⁷D. Iliescu, D. Cullen, and I. Baker, *Cold Reg. Sci. Eng.* **35**, 81 (2002).
- ³⁸I. Baker, D. Cullen, and D. Iliescu, *Can. J. Phys.* **81**, 1 (2003).
- ³⁹D. Beaglehole, *J. Cryst. Growth* **112**, 663 (1991).
- ⁴⁰J. Weiss, J. Vidot, M. Gay, L. Arnaud, P. Duval, and J. R. Petit, *Ann. Glaciol.* **35**, 552 (2002).
- ⁴¹H. Eicken, H. Oerter, H. Miller, W. Graf, and J. Kipfstuhl, *J. Glaciol.* **40**, 135 (1994); **40**, 386 (1994).
- ⁴²K. M. Cuffey, H. Conway, A. Gades, B. Hallet, C. F. Raymond, and S. Whitlow, *J. Geophys. Res.* **105**, 27895 (2000).
- ⁴³H. J. V. Tyrrell and K. R. Harris, *Diffusion in Liquids: A Theoretical and Experimental Study* (Butterworths, London, 1984).
- ⁴⁴G. E. Murch, *Diffusion in Solids: Unsolved Problems* (Trans Tech, Zurich, 1992).
- ⁴⁵J. Kärger, P. Heitjans, and R. Haberlandt, *Diffusion in Condensed Matter* (Vieweg, Braunschweig, 1998).
- ⁴⁶G. E. Murch and A. S. Nowick, *Diffusion in Crystalline Solids* (Academic, Orlando, FL, 1984).
- ⁴⁷P. Sachtchenko, *Philos. Mag. Lett.* **80**, 627 (2000).
- ⁴⁸P. G. Shewmon, *Diffusion in Solids* (The Minerals, Metals & Materials Society, Warrendale, Pa, 1989).
- ⁴⁹L. A. Wilen and J. G. Dash, *Science* **270**, 5239 (1995).
- ⁵⁰N. E. Munoz, S. R. Gilliss, and C. Barrycarter, *Philos. Mag. Lett.* **84**, 21 (2004).
- ⁵¹W. W. Mullins, *J. Appl. Phys.* **28**, 333 (1957).
- ⁵²S. Ogawa, T. Yoshida, and T. Kouzaki, *Appl. Phys. Lett.* **56**, 725 (1989).
- ⁵³D. J. Srolovitz and S. A. Safran, *J. Appl. Phys.* **60**, 247 (1986).
- ⁵⁴T. P. Nolan and R. Sinclair, *J. Appl. Phys.* **71**, 720 (1992).
- ⁵⁵V. Sadtchenko and G. E. Ewing, *Langmuir* **18**, 4632 (2002).
- ⁵⁶S. P. William, H. Ide, and Y. Arata, *J. Phys. Chem. A* **103**, 448 (1999).
- ⁵⁷H. Z. Weingartner, *Z. Phys. Chem., Neue Folge* **132**, 129 (1982).
- ⁵⁸H. R. Pruppacher, *J. Chem. Phys.* **56**, 101 (1972).
- ⁵⁹K. T. Gillen, D.C. Douglass, and M. J. R. Hoch, *J. Chem. Phys.* **57**, 5117 (1972).
- ⁶⁰Y. Furukawa, M. Yamamoto, and T. Kuroda, *J. Cryst. Growth* **82**, 665 (1987).
- ⁶¹J. G. Dash, *Contemp. Phys.* **30**, 89 (1989).